



Using Commercial Aircraft Meteorological Data to Assess the Heat Budget of the Convective Boundary Layer Over the Santiago Valley in Central Chile

Ricardo C. Muñoz¹ · C. David Whiteman² · René D. Garreaud³ · José A. Rutllant⁴ · Jacqueline Hidalgo⁵

Received: 7 April 2021 / Accepted: 14 December 2021 / Published online: 7 January 2022
© The Author(s) 2022

Abstract

The World Meteorological Organization Aircraft Meteorological Data Relay (AMDAR) programme refers to meteorological data gathered by commercial aircraft and made available to weather services. It has become a major source of upper-air observations whose assimilation into global models has greatly improved their performance. Near busy airports, AMDAR data generate semi-continuous vertical profiles of temperature and winds, which have been utilized to produce climatologies of atmospheric-boundary-layer (ABL) heights and general characterizations of specific cases. We analyze 2017–2019 AMDAR data for Santiago airport, located in the centre of a $40 \times 100 \text{ km}^2$ subtropical semi-arid valley in central Chile, at the foothills of the Andes. Profiles derived from AMDAR data are characterized and validated against occasional radiosondes launched in the valley and compared with routine operational radiosondes and with reanalysis data. The cold-season climatology of AMDAR temperatures reveals a deep nocturnal inversion reaching up to 700 m above ground level (a.g.l.) and daytime warming extending up to 1000 m a.g.l. Convective-boundary-layer (CBL) heights are estimated based on AMDAR profiles and the daytime heat budget of the CBL is assessed. The CBL warming variability is well explained by the surface sensible heat flux estimated with sonic anemometer measurements at one site, provided advection of the cool coastal ABL existing to the west is included. However, the CBL warming accounts for just half of the mean daytime warming of the lower troposphere, suggesting that rather intense climatological diurnal subsidence affects the dynamics of the daytime valley ABL. Possible sources of this subsidence are discussed.

✉ Ricardo C. Muñoz
rmunoz@dgf.uchile.cl

¹ Department of Geophysics, University of Chile, Santiago, Chile

² Department of Atmospheric Sciences, University of Utah, Salt Lake City, USA

³ Department of Geophysics, University of Chile and Center for Climate and Resilience Research (CR2), Santiago, Chile

⁴ Department of Geophysics, University of Chile and Centre for Advanced Studies in Arid Zones (CEAZA), La Serena, Chile

⁵ Dirección Meteorológica de Chile, Santiago, Chile

Keywords Aircraft Meteorological Data Relay (AMDAR) programme · Convective boundary layer · Heat budget · Santiago, Chile · Valley boundary layer

1 Introduction

The global Aircraft Meteorological Data Relay (AMDAR) programme is a World Meteorological Organization effort to collect meteorological data gathered by commercial aircraft around the world and make the data available to meteorological services (Moninger et al. 2003; Petersen 2016). The programme has greatly expanded the global availability of meteorological observations in the vertical beyond the historical global radiosonde network and its assimilation into global weather forecasting models has produced significant improvements in their performance (Cardinali et al. 2003; Petersen 2016). More recently, the use of AMDAR data in characterizing the atmospheric boundary layer (ABL) over various regions has been documented. Rahn and Mitchell (2016) used AMDAR data to characterize and understand the diurnal climatology of the coastal ABL in California, considering it to be a promising source of ABL information near busy airports where AMDAR data are available almost continuously in time. Zhang et al. (2019) evaluated the quality of AMDAR low-level vertical profiles by comparing them with nearby radiosondes for 54 U.S. airports. This work included also a comprehensive review of previous evaluations of AMDAR data and confirmed it to be well suited for ABL studies. Similar conclusions were obtained by Ding et al. (2015) and Ding et al. (2018) in studies conducted over China. Zhang et al. (2020a) produced a comparative climatology of ABL heights over the U.S., discussing different methods to diagnose them and comparing the results with those from ERA5 reanalyses and short-term field campaigns. Other more specific uses of AMDAR data in ABL studies include the evaluation of their performance to detect inversion and shear layers at an airport (Drüe et al. 2010) or the sensitivity of the ABL to heat waves (Zhang et al. 2020b). Despite these efforts, the use of AMDAR data in ABL studies can still be considered as incipient, especially in more quantitative evaluations of the mechanisms affecting the ABL dynamics in specific settings. In this regard, the potential of having publicly available long-term, semi-continuous, high-resolution vertical profiles of temperature and winds near the surface has not yet been fully realized.

At the end of 2016 the South American LATAM airlines group joined the AMDAR programme with funding from the U.S. AMDAR-Meteorological Data Collection and Reporting System (MDCRS) program (WMO 2017). As a result, the availability of vertical profiles of meteorological variables at many regional sites increased dramatically. We concentrate our analysis on the AMDAR data associated with the Santiago international airport located in Santiago valley to provide new observational information on its climatology and associated physical mechanisms. From an applied perspective, Santiago's ABL is important in modulating the very serious air pollution problem affecting the health and life quality of its 6 million residents (Koutrakis et al. 2005). From a more general perspective, the Santiago valley constitutes a complex terrain ABL that develops at the foot of the Andes mountains and relatively close to the ocean so that interactions between coastal and valley ABLs and between sea- and valley-breeze systems can be expected. These complexities are compensated by a semi-arid surface, a very stable subtropical climate and considerable topographic confinement, especially during non-disturbed days in the cold season when, as shown below, the convective boundary layer (CBL) develops generally within the valley. For this reason the scope of the present work is focused on the April–September period, coincident also with the particulate-matter air pollution season of the city (Muñoz 2012).

Valley heat budgets and their relationship to valley wind systems have a long history of research, which has been reviewed by Whiteman (1990) and Zardi and Whiteman (2013). The relatively simple heating mechanism of a flat horizontally homogeneous CBL driven by the vertical convergence of turbulent heat fluxes (Tennekes 1973) is complicated in valleys due to the three-dimensional geometry of the terrain and the vertical and horizontal advection associated with mesoscale circulations induced by the differential heating of the surfaces and the dynamical interactions of the flow with the topography. More recently, De Wekker and Kossmann (2015) and Lehner and Rotach (2018) reviewed the challenges of defining the ABL top over mountainous terrain and its importance in influencing the exchanges between complex terrain and the free atmosphere. Here, the turbulent layer near the surface warmed primarily by the surface sensible heat flux is called the mixed layer or CBL, and following Lehner and Rotach (2018), we designate the lower part of the troposphere showing significant daytime warming as the mountain boundary layer (MoBL). As argued by these authors, despite not being always fully turbulent, the MoBL still falls within the Stull (1988) definition of an ABL.

Our goals are: (1) to validate and utilize AMDAR data to characterize the diurnal climatology of the Santiago valley MoBL, (2) to test whether the AMDAR data can be used to constrain the heat budget of the Santiago valley MoBL, and (3) to identify the main factors controlling that budget as suggested by the new data. Section 2 describes the site, climate and the data used. Section 3 documents in more detail the AMDAR data and provides comparisons with radiosondes and model reanalyses. Section 4 presents a 3-year climatology of AMDAR data and in Sect. 5 we assess the daytime heat budget for the Santiago CBL. The last two sections are devoted to discussions and conclusions.

2 Site and Data

2.1 Site and Climate

The focus of this study is the MoBL developing over the Santiago valley of central Chile in the western foothills of the subtropical Andes (Fig. 1). The valley extends about 100 km in the north–south direction and about 40 km in the east–west direction, with its floor ranging from about 300 m above sea level (a.s.l.) in its south-western corner up to about 800 m a.s.l. on its eastern flank. The valley limit to the east is the Andes Cordillera, which at these latitudes rises above 5000 m a.s.l. To the west the coastal range produces hills surpassing 1000 m a.s.l. while to the north and south narrow passes connect the valley to the Aconcagua and Cachapoal valleys, respectively. The main connection of the Santiago valley with the cool coastal ABL existing to the west is through its south-western corner (point 5 in Fig. 1), through which the Maipo river with its head in the Andes runs its course into its mouth near the Santo Domingo township at the coast (point 6 in Fig. 1).

The urban land cover of the valley occupies its central portion and encompasses roughly one third of the area. Rural regions to the north and south are dominated by open grasslands/shrublands and agricultural land, respectively (Peña 2008; Bustos and Meza 2015).

At 33.5°S and 70.7°W, the Santiago valley has a subtropical semi-arid (310 mm mean annual rainfall) climate dominated by the south-east Pacific anticyclone. Its attendant regional-scale subsidence provides for very stable conditions prevailing in the lower troposphere, modulated by the intensity and position of the anticyclone and disrupted by the occasional arrival of mid-latitude perturbations in the cold season (Garreaud 2013). Under

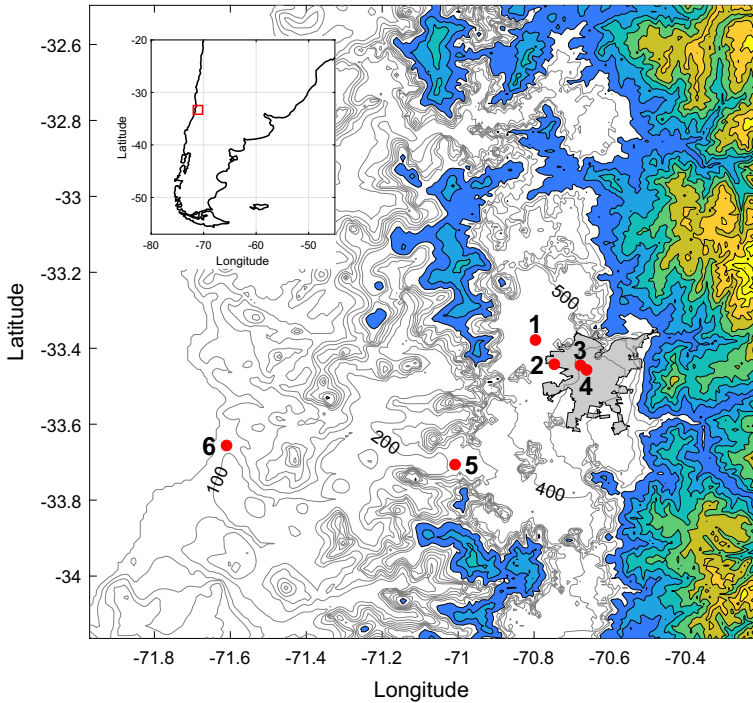


Fig. 1 Topography of the Santiago valley and surroundings. Grey contours from 0 to 800 m a.s.l. every 100 m. Coloured contours from 1000 to 5000 m a.s.l. every 500 m. Red circles mark locations of measuring points: 1: Santiago airport (SCEL), 2: DASA tower, 3: Quinta Normal (SCQN), 4: Department of Geophysics (DGF), 5: El Paico station, 6: Santo Domingo operational radiosonde station (SCSN). The shaded area in the valley marks the urban region of Santiago city. The red box in the inset shows the location of the study area in southern South America

more unperturbed conditions, a major factor in the central Chile weather is the frequent development of coastal lows propagating poleward at a quasi-weekly pace (Rutllant and Garreaud 1995; Garreaud et al. 2002). These systems produce large variations of the lower tropospheric stability under which the Santiago MoBL develops. In terms of winds, the topographic confinement and the large stability sustain a valley-breeze system characterized at the surface by south-westerly winds in the afternoon and very weak downslope winds at night (Rutllant and Garreaud 2004; Muñoz and Corral 2017).

2.2 Aircraft Data

The AMDAR data used here have been retrieved from the National Oceanic and Atmospheric Administration (NOAA) Earth System Research Laboratory/Global Systems Division (GSD) webpage (<https://ruc-soundings.noaa.gov/>) (Moninger et al. 2003), which provides soundings based upon aircraft meteorological data acquired in the climbing and descent phases of flights. For the full 2017–2019 period, a grand total of 106,608 soundings were available for the Santiago airport (SCEL). Although GSD data have already been subject to quality control, we applied additional filters to make sure the resulting database is best suited for our boundary-layer analyses. Specifically, we demanded that, in terms of the standard height to

be defined in the next paragraph, the lowest height of the data is between 300 and 600 m a.s.l., the highest data level is above 4000 m a.s.l., the sounding has six or more data levels below 3000 m a.s.l., and the temperature profile does not differ more than 5 °C from the median of all AMDAR soundings in a 4-h window around it. These conditions discarded 2.5% of the soundings and left 103,976 for subsequent analysis.

The main vertical coordinate of AMDAR data is pressure. The soundings also include a standard height coordinate, which is the altitude that a standard atmosphere has at the corresponding pressure. Following Rahn and Mitchell (2016), we give preference to a height coordinate computed by integrating the hypsometric equation over each sounding. As the initial point of the integration, we used the first level of the sounding when its pressure was at most 2 hPa less than the surface pressure of the airport meteorological station (73.1% of soundings). In the remaining cases, we extended the soundings by adding a bottom data level with temperature and winds reported by the airport surface station.

In terms of vertical resolution, most of the soundings have between 12 and 17 data points below 3000 m a.s.l., which is equivalent to an average vertical resolution between 150 and 200 m. Similar to Rahn and Mitchell (2016) and Zhang et al. (2020a), each temperature and wind component vertical profile was linearly interpolated onto a regular vertical grid with 25-m resolution and then all soundings in every hour were averaged to produce the basic hourly database analyzed. In the cold season an overall 89% time coverage is achieved, which decreases to about 70% between 0100 and 0600 LT (local time = UTC - 4 h). As the nominal altitudes of the SCEL airport landing track and the surface meteorological station are 476 and 482 m a.s.l., respectively, the first data level of AMDAR soundings was truncated at 500 m a.s.l. Unless stated otherwise, height coordinates of vertical profiles are expressed as heights above ground level (a.g.l.) using 500 m as the offset with respect to heights a.s.l. With respect to the time convention, unless otherwise noted, local time is used. We note that for the longitude of Santiago a better approximation to solar time would be UTC - 5 h, but UTC - 4 h is used to match the official time in Chile during the cold season. Further characterization of the AMDAR dataset dealing with its special features is provided in Sect. 3.1.

2.3 Ancillary Data

Two sets of radiosondes are used to compare against AMDAR profiles. The most comparable set corresponds to radiosondes launched occasionally by the Chilean Weather Service (DMC) from station SCQN in the Santiago valley in support of the management of the air pollution problem of the city (point 3 in Fig. 1). In this case we have available 33 soundings released on different days between April and October of years 2017–2019 at various hours between 0800 and 1200 LT. Twelve of them have data with 30-s resolution (\approx 150-m resolution) and 21 have only the sounding message with mandatory and significant levels.

The second set corresponds to 1200 UTC operational radiosondes launched daily from the Santo Domingo airfield (SCSN) located at the coast about 100-km west of Santiago (point 6 in Fig. 1), and were downloaded from the University of Wyoming (<http://weather.uwyo.edu/upperair/sounding.html>), including mandatory and significant levels of temperature and winds.

A ceilometer (Model CL31, Vaisala Oyj, Vantaa, Finland) operates continuously over the Department of Geophysics (DGF) building in downtown Santiago (point 4 in Fig. 1). During cloudless conditions, ceilometer reflectivity profiles describe the aerosol dynamics in the boundary layer and have been used to derive estimates of the height of the Santiago daytime mixed layer (Muñoz and Undurraga 2010).

Surface meteorological stations used here include the official SCEL airport station, the El Paico station located at the south-western entrance of the valley and the Department of Airfields and Aeronautical Services (DASA) tower. The latter is a 30-m micrometeorological mast from which we use data obtained at 10 m a.g.l. with a sonic anemometer (Model 81000, R. M. Young Co., Traverse City, Michigan, USA). In particular we use turbulent covariances of sonic temperature and vertical velocity component measured at 1 Hz as an estimate of the surface sensible heat flux exchanged between the surface and the boundary layer. While a 1 Hz sampling rate may be too small for some turbulence analyses, Bosveld and Beljaars (2001) showed that for estimating multi-hour flux averages like those used here, 1 Hz and 10 Hz measurement rates produce almost identical estimates. Using the tool of Kljun et al. (2015), the 70% contour of the cold-season daytime footprint of these measurements encompasses in similar fractions a plot of bare soil to the south-west of the tower and a sector of single-floor houses with little green coverage to the north. The locations of the three surface sites are shown also in Fig. 1. Their operation is the responsibility of the DMC and the data are available from its website (<https://climatologia.meteochile.gob.cl/>).

Beyond observations, we also compare AMDAR profiles with ERA5 model reanalyses, using hourly outputs with 0.25° horizontal resolution available from the Copernicus website (<https://cds.climate.copernicus.eu/>) (Hersbach et al. 2018). In particular, we use results for the grid point located at 33.50°S and 70.75°W and consider pressure levels from 1000 to 750 hPa every 25 hPa plus the 700, 600, and 500 hPa levels.

2.4 Convective-Boundary-Layer-Height Estimates

Radiosonde and AMDAR data have been used to produce ABL height climatologies over several regions (Seidel et al. 2010; Zhang et al. 2020a). The cited references provide inter-comparisons of various methods to derive ABL heights, some of which rely solely on the temperature profile while others also include the wind profile and surface data. We consider here two methods for this purpose. The first is the algorithm based on a bulk Richardson number (Ri_b) computed from the AMDAR temperature and wind profiles. In particular, we use the implementation found to be the best by Zhang et al. (2020a), who compute Ri_b with the expression

$$Ri_b = \frac{(g/\theta_{vs})(\theta_{vz} - \theta_{vs})(z - z_s)}{(u_z - u_s)^2 + (v_z - v_s)^2 + bu_*^2}, \quad (1)$$

where θ_{vz} , u_z , and v_z (θ_{vs} , u_s , and v_s) are virtual potential temperature, zonal, and meridional wind components at height z (z_s), respectively; u_* is the surface friction velocity; g is the acceleration due to gravity; and b is an empirical coefficient (Vogelezang and Holtslag 1996). The ABL height is found at the lowest level where $Ri_b = Ri_c$, where Ri_c is a critical Richardson number. We implemented the method using parameters following Zhang et al. (2020a): $b = 100$, $Ri_c = 0.5$. For surface variables we used data from the airport meteorological station, except for u_* , which was obtained from the DASA tower. The virtual correction was omitted due to lack of humidity information in the AMDAR profiles.

As a second method, we use the so-called parcel method (Seibert et al. 2000; Seidel et al. 2010), in which the CBL height is defined by the level at which the vertical profile of potential temperature has the same value as at the surface, the latter according to the airport surface meteorological station. Seibert et al. (2000) point out that by not considering winds, the parcel method is best suited for unstable conditions like those of interest here, and while advanced formulations have been proposed in which corrections for the surface temperature

are considered, we implemented the simplest version of the method with no correction. With both methods, once the CBL height, h , is found, its potential temperature, θ , is defined simply as the average of the potential temperature in the layer between the surface and this level. To reduce data gaps, 1-h missing values of h and θ were filled with simple time interpolation.

Use of lidar ceilometers to derive CBL heights has increased in recent years (Emeis et al. 2008). For the case of Santiago, Muñoz and Undurraga (2010) applied an algorithm to derive daytime mixed-layer heights based upon the shape of the DGF ceilometer backscatter intensity profiles for cloudless conditions. These ceilometer-derived heights are compared in Sect. 4.2 with those obtained from the AMDAR data using the two methods described previously. The ceilometer-derived heights are used solely as reference to the AMDAR-based retrievals, because being dependent on the aerosol load of the ABL they are many times hard to define early in the morning (due to complex aerosol layers) and late in the afternoon (due to diluted aerosol loads), thus producing a rather incomplete time series (Muñoz and Undurraga 2010). We emphasize also that the main focus of this paper is not a comprehensive and detailed intercomparison of CBL height estimation methodologies, as has been performed by others, but the use of CBL heights estimated with AMDAR data in assessing the physical factors that control the daytime MoBL heat budget over Santiago.

3 Aircraft Data Characterization and Validation

3.1 Temporal and Spatial Coverage

The number of flight operations at an airport has a strong variation that impacts the hourly availability of soundings. At the SCEL airport the global average number of AMDAR soundings per hour was four, increasing up to 5.5 h^{-1} in the 1300–1800 LT period and decreasing to 2 h^{-1} between 0100 and 0600 LT. This night-time reduced availability has effects on the robustness and noise of climatological averages during these hours, as shown below. In terms of the availability of soundings throughout the year, the SCEL airport has an average of 95 soundings per day, which increases to 104 in the warm months (October–March) and decreases to 86 in the cold months (April–September). Finally, the number of soundings for years 2017, 2018, and 2019 are 39642, 36198, and 28136, respectively.

Aircraft soundings probe the atmosphere along the slant path followed by the airplane when it takes off from or lands at an airport. As a result, the measuring path is much more inclined than the typical path of a routine radiosonde. Thus, proper interpretation of AMDAR soundings may have to consider the position of the aircraft at every data point in the sounding. This task is facilitated in the GSD database because each sounding is declared as an ascent or descent sounding and each data point includes the corresponding range and bearing of the aircraft position with respect to the airport. In the case of the SCEL airport, the two landing tracks have a north–south orientation and the surface wind climatology ensures that the vast majority of aircraft approach the airport from the north and take off toward the south. Thus, at 850 hPa ($\approx 1000 \text{ m a.g.l.}$) the ascent (descent) sounding data points most commonly have bearings around 180° (0°) and ranges between 10 and 15 km (20–25 km) with respect to the airport. Later in the flight, at 700 hPa ($\approx 2500 \text{ m a.g.l.}$), aircraft positions are more varied: on ascents the ranges are between 15 and 35 km and about half of cases have a southerly bearing (planes presumably with a destination to the south of the country) and the other half have a south–west–west bearing (planes presumably taking routes to the north of the country). On descent, 15% of soundings have a range between 0 and 10 km (planes overpassing the airport

to land from the north) and the rest have ranges between 50 and 70 km and a northerly bearing. With the Santiago valley extending about 100 km in the north–south direction and the airport located near the centre of the valley (Fig. 1), these ranges and bearings show that below ≈ 2000 m a.g.l. the measurements are indeed taken inside the valley's airmass. Moreover, as descents and ascents are very close in number and they probe mostly the northerly and the southerly portion of the valley, respectively, the simple averages with no distinction between ascents and descents are considered to best represent the conditions over the bulk of the valley and will be used as such in this paper. The same decision was made by Rahn and Mitchell (2016) and Zhang et al. (2019). Still, the comparison between hourly vertical profiles computed solely with ascent or descent soundings shows a mean temperature bias $\approx 1^\circ\text{C}$ near the surface and $< 0.5^\circ\text{C}$ above 500 m a.g.l. (descents warmer than ascents) and root-mean-squared deviations (r.m.s.d.) less than 1°C below 4000 m a.s.l. For zonal and meridional winds, mean biases are $\approx 1\text{ m s}^{-1}$ at ≈ 500 m a.g.l. and close to zero between 2000 and 4000 m a.s.l., with r.m.s.d. $\approx 2\text{ m s}^{-1}$ in that layer. We note that our ascent–descent thermal bias is opposite to that quoted for previous studies by Moninger et al. (2003) in which ascent temperatures are on average 0.4°C warmer than descent values, but they agree with the typical meridional daytime thermal gradient over the Santiago valley as derived from satellite observations by Bustos and Meza (2015). In Sect. 5 we explore the possibility of using the ascent–descent temperature differences to estimate meridional thermal advection in the valley. A more thorough study of the ascent–descent differences in temperature and wind profiles is, however, left for future work.

3.2 Validation

3.2.1 Comparison with Santiago Radiosondes

As mentioned in Sect. 2, we have available 33 cold-season morning radiosondes launched from a site in the valley about 11-km south-east of the airport, which we use to compare with AMDAR soundings as a limited-scope validation of the latter. As an example, Fig. 2 shows vertical profiles of temperature (T) and wind for the radiosonde of 1100 LT 8 August 2018 (blue lines) together with the five AMDAR soundings at that hour (grey lines) and the averaged AMDAR profiles (red lines). It is apparent in this case that the radiosonde profiles fall well inside the variability among individual AMDAR soundings and that the averaged AMDAR profiles approximate well the radiosonde profiles. The generalization of the comparison is presented in Fig. 3. Panel a shows a very good correspondence between the averaged vertical temperature, zonal, and meridional wind profiles obtained from the radiosondes (blue) and from the AMDAR soundings (red). Only very close to the surface is there a bias in temperature, probably due to the separation between launching sites. Figure 3b shows vertical profiles of correlations between the radiosondes and the AMDAR soundings for the three main variables. Temperatures are strikingly well correlated between both data sources, with a slight decrease near the surface. In contrast, correlations between wind components are smaller, especially below 1000 m a.g.l. At these heights, located below the topography surrounding the Santiago valley, the mean winds are weak (Fig. 3a) and inside-valley meso- γ or finer variability may explain the smaller correlation between both data sources. Finally, Fig. 3c shows vertical r.m.s.d. profiles of the comparisons. Typical differences in temperature between radiosondes and AMDAR profiles are ≈ 0.5 – 1°C , except near the surface where they increase up to 2°C . Typical differences in wind components, on the other hand, are between 1 and 2 m s^{-1} , which below 1000 m a.g.l. is comparable to the mean values and

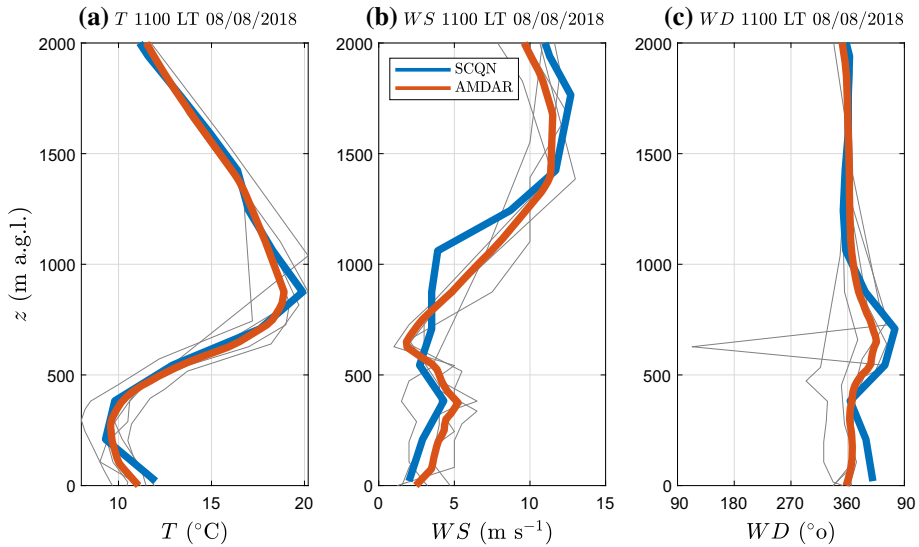


Fig. 2 Example comparison of AMDAR profiles and radiosondes launched from SCQN station on 8 August 2018 at 1100 LT (blue lines). The red line marks the hourly AMDAR average computed over five individual soundings available for this time shown with fine grey lines. **a** Temperature (T), **b** wind speed (WS), and **c** wind direction (WD)

further explains the lack of correlation of wind components at these levels noted in Fig. 3b. In general, the results in Fig. 3 fall within those of the comprehensive radiosondes–AMDAR comparison documented by Zhang et al. (2019), who, for collocated sites and altitudes below 850 hPa, found temperature (wind components) r.m.s.d. and mean biases values of $1.3\text{ }^{\circ}\text{C}$ (2.2 m s^{-1}) and less than $0.32\text{ }^{\circ}\text{C}$ (0.7 m s^{-1}), respectively.

3.2.2 Comparison with Santo Domingo Radiosondes and ERA5 Reanalysis

We further compare in Fig. 4 the AMDAR soundings at 1200 UTC (0800 LT, early morning) with the corresponding Santo Domingo (SCSN) operational radiosondes and with ERA5 reanalyses for the grid point closest to Santiago airport. More than a validation, the aim of these comparisons is to show the added value of the AMDAR soundings with respect to the closest historically available upper-air observations (SCSN) and commonly used reanalyses (ERA5). Additionally, the comparison between the SCSN and AMDAR soundings sheds light on the regional-scale controls affecting the inter-daily variability of the Santiago ABL. Figure 4a shows mean profiles of temperature, and zonal and meridional winds obtained with the three data sources for the cold period (488 days with data). The comparison of AMDAR and SCSN temperatures shows that between 1000 and 2000 m a.g.l. AMDAR profiles have a slight ($\approx 1\text{ }^{\circ}\text{C}$) warm bias with respect to the SCSN profiles. This bias diminishes aloft but changes sign and increases towards the surface. Below 500 m a.g.l., the mean SCSN temperature profile is mostly isothermal down to sea level, where a shallow surface inversion is present. The AMDAR temperature profile shows instead a well-defined inversion layer between the valley surface and $\approx 700\text{ m a.g.l.}$ The differences between AMDAR and SCSN mean temperature profiles below 1000 m a.g.l. probably reflect the very different boundary layers that each sounding is probing: while the SCSN station measures a coastal marine

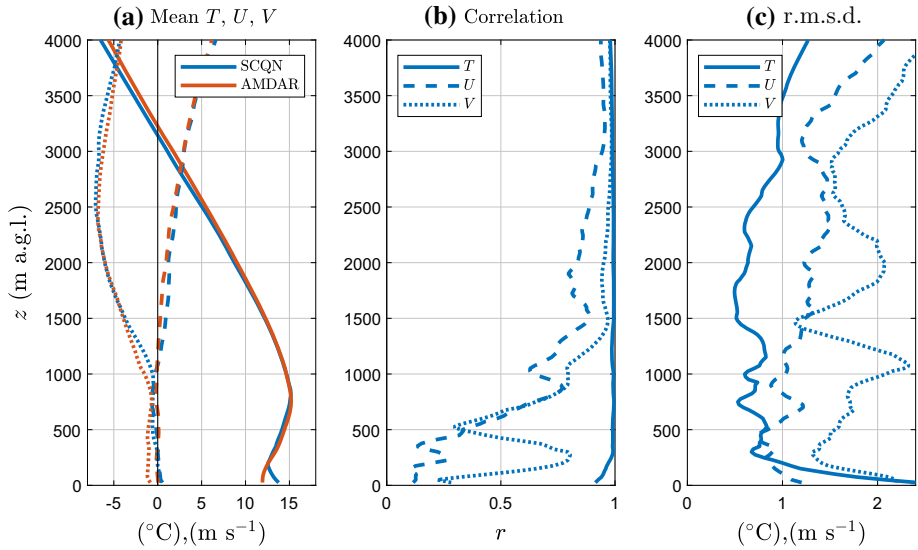


Fig. 3 Comparison between AMDAR hourly profiles and 33 radiosondes launched from SCQN station on different days of April–October 2017–2019 between the hours of 0800 and 1200 LT. **a** Mean profiles of temperature (continuous), zonal wind (dashed), and meridional wind (dotted). Blue lines are for SCQN radiosondes and red lines for AMDAR profiles. **b** Linear correlation factors (r) for temperature (continuous), zonal wind (dashed), and meridional wind (dotted). **c** as (b) but for root mean squared deviations

boundary layer capped frequently by a marked subsidence inversion that varies synoptically in terms of height and strength, AMDAR profiles at these altitudes describe the airmass inside the Santiago valley, which is subject to extra cooling during the night. The comparison of mean temperature profiles between AMDAR and ERA5 reanalyses, on the other hand, is disappointing below 1000 m a.g.l. where the reanalyses are unable to capture the inversion layer near the surface. This is probably due to the still rather coarse resolution of the reanalyses and the fact that the physical mechanisms producing the cold pool of the Santiago valley are tied to the local topography of the valley and its surroundings, which ERA5 does not simulate well.

In terms of wind components, the three data sources produce very similar mean vertical profiles in the entire altitude range shown (Fig. 4a). The small mean winds below 1000 m a.g.l., already noted in the previous section, are observed over Santiago and at the coast and are also reproduced by the reanalyses. Aloft, the increase of the zonal wind with altitude is consistently shown by the three profiles, while the northerly flow that peaks around 2500 m a.g.l. is also present in all of them. This latter feature of the climatological regional winds has been attributed to a blocking effect of the Andes Cordillera to the east (Kalthoff et al. 2002; Rutllant and Garreaud 2004; Scaff et al. 2017), which may explain the larger northerly winds of the AMDAR and ERA5 profiles as compared to the SCSN profile.

Figure 4b shows vertical profiles of correlation coefficients between AMDAR and ERA5 data (red) and between AMDAR and SCSN profiles (yellow). As was the case with the Santiago soundings, temperature correlations are very close to 1 above 1000 m a.g.l., but decrease towards the surface, reaching in this case much reduced surface correlations. This drop in correlation can be interpreted as the effect of local valley processes not present at the coast (AMDAR–SCSN comparison) and as the inability of the reanalysis to reproduce

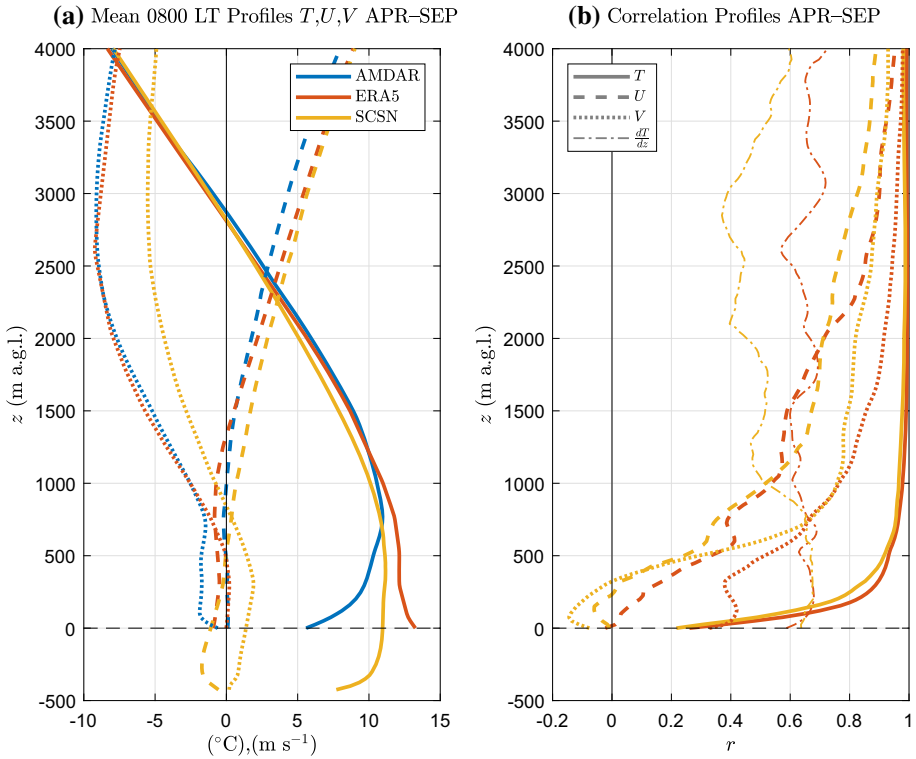


Fig. 4 Comparison between 0800 LT (1200 UTC) AMDAR profiles, SCSN radiosoundings, and ERA5 profiles for 488 days in April–September (APR–SEP) 2017–2019 in which all three datasets have information. **a** Mean vertical profiles of temperature (continuous), zonal wind (dashed), and meridional wind (dotted). Blue, red, and yellow denote AMDAR, ERA5, and SCSN vertical profiles, respectively. **b** Correlation coefficients for temperature (continuous), zonal wind (dashed), meridional wind (dotted), and 500-m layer temperature gradient dT/dz (dot-dashed). Red (yellow) lines denote AMDAR–ERA5 (AMDAR–SCSN) correlations. In both panels the vertical coordinate is referenced to Santiago ground level (black dashed horizontal lines). It was extended to -500 m to include the full SCSN profiles which begin near sea-level

them (AMDAR–ERA5 comparison). We also computed correlations between temperature gradients in 500-m layers (fine dash-dotted lines) as a means of describing the stability co-variability of the three data sources. As expected, the correlation coefficients for stability are generally smaller than for temperature, but it is interesting to note that, unlike for temperature, they do not decrease towards the surface. Indeed, the correlation between AMDAR and SCSN stability increases from 0.4 aloft up to almost 0.7 near the surface. Thus, the 500-m scale stability in the Santiago valley appears to vary synoptically in concert with the regional stability and this variability is partially reproduced by the reanalysis. In terms of wind components, the correlation profiles of Fig. 4b also show a significant decrease below 1000 m a.g.l. as compared to the values aloft. This is probably because low-level winds at the coast and in the Santiago valley respond differently to similar regional synoptic forcings and because the reanalysis is unable to reproduce well the valley wind circulation. In conclusion, while above 2000 m a.g.l. the three datasets are very comparable, below 1000 m a.g.l. the AMDAR profiles provide information on the valley circulation and thermal structure not contained in the coastal radiosondes nor in the reanalysis.

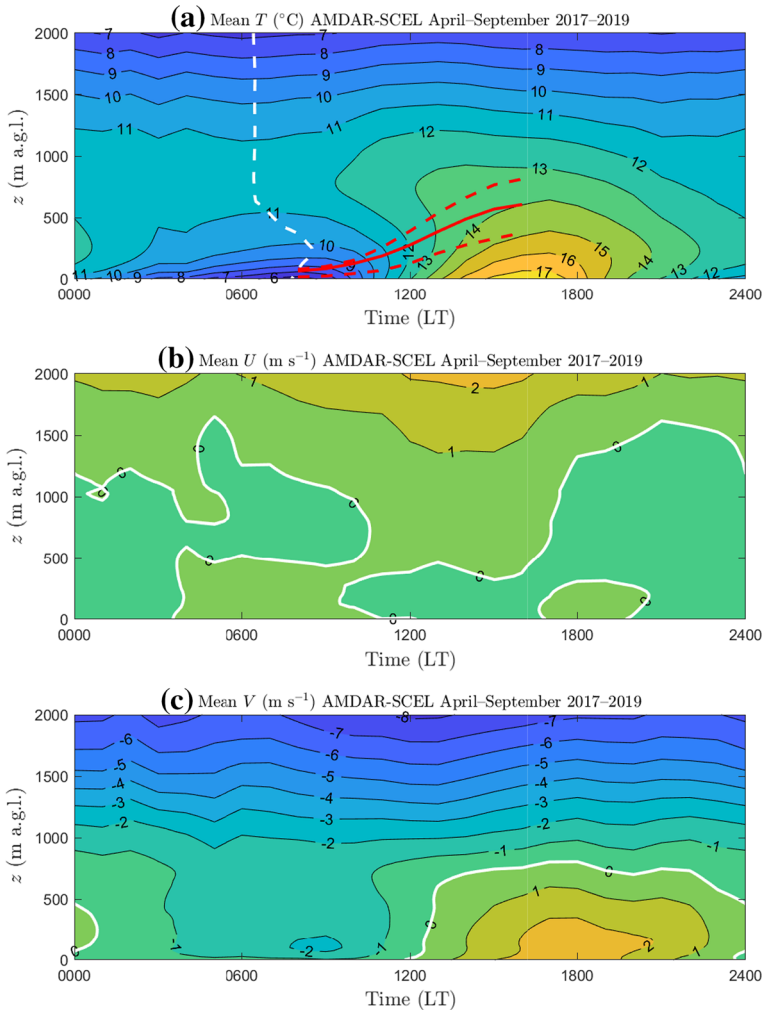


Fig. 5 Mean time-height cross-sections of AMDAR data for Santiago for April–September 2017–2019. **a** Temperature ($^{\circ}\text{C}$). Dashed white line marks the occurrence of the minimum morning temperature. Red lines mark mean (continuous) and upper and lower quartiles (dashed) of 0800–1600 LT CBL heights computed with the Ri_b method. **b** Zonal wind (m s^{-1}). **c** Meridional wind (m s^{-1}). In (**b**) and (**c**) the zero-contour has been highlighted with a bold white line

4 Santiago Mountain Boundary Layer Characterized with Aircraft Data

4.1 Mean Diurnal Cycles

Santiago AMDAR data provide an unprecedented monitoring of temperature and winds in the valley's air mass, from which their cold-season (April–September) mean diurnal cycles in the first 2000 m a.g.l. are shown in Fig. 5. We have left out of this and all subsequent analyses 71 days with rain measured at the SCQN station, leaving a maximum of 478 days to consider, although in some analyses missing data will reduce the number further. Diurnal

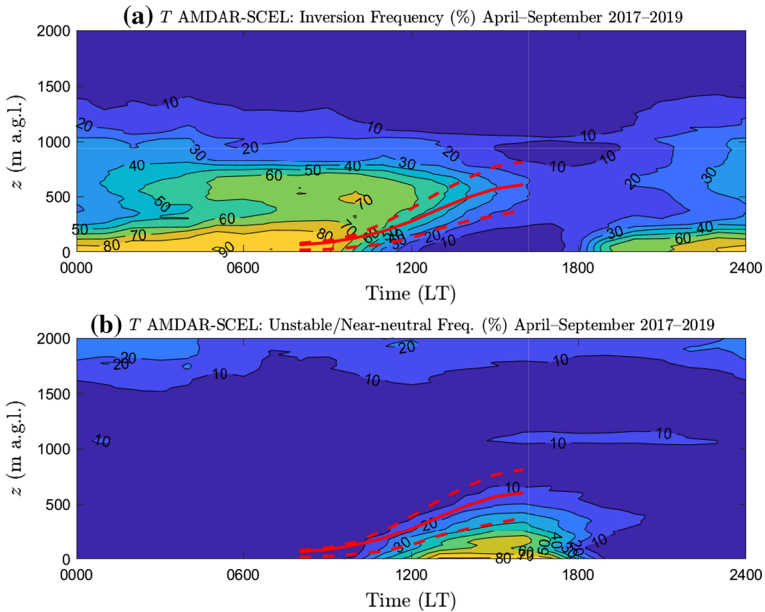


Fig. 6 Time-height cross-sections of the frequency (%) of temperature inversions (a) and unstable and near-neutral layers (b) based upon AMDAR data for Santiago in April–September 2017–2019. Red lines as in Fig. 5a

heating in Fig. 5a reaches on average up to about 1000 m a.g.l., while the mean nocturnal surface inversion has a depth of more than 500 m and a strength of about 6°C , although we point out that the air layer very close to the surface is not fully included in these data (Sect. 2) so that the intensity of the nocturnal surface-based inversion is underestimated. Above the inversion, a mean isothermal layer develops during the night, with some noise presumably due to the reduced number of soundings available between 0100 and 0600 LT. Interestingly, during the morning transition, warming is intense near the surface but it is appreciable also in the full 1000-m layer closest to the ground, even above the typical daytime CBL (red lines). This deep morning warming cannot be fully explained by the surface sensible heat flux, as documented and discussed later.

Zonal winds are on average very weak in the 2000-m layer close to the surface (Fig. 5b). Meridional winds, on the other hand, show a marked near-surface diurnal cycle with larger positive values (southerly winds) during daytime and weak negative values in the night (Fig. 5c). Above 1000 m a.g.l. negative meridional winds dominate all day related to the northerly blocking jet mentioned earlier.

Beyond the characterization of mean temperatures, the diurnal variation of stability over Santiago is described in Fig. 6 by means of the frequency of occurrence of inversion layers ($dT/dz > 0$, panel a) and of unstable and near-neutral layers ($d\theta/dz < 0.002 \text{ K m}^{-1}$, panel b). As expected, inversion frequencies maximize near the surface during the night, when a $\approx 100\text{-m}$ layer shows inversions more than 80% of the time. A secondary maximum of inversion frequency above 60% is observed around 500 m a.g.l. between 0500 and 1200 LT. Its detachment from the near-surface inversion frequency maximum suggests that it responds to mechanisms beyond surface cooling, like for example the influence of the regional subsidence inversion (Gramsch et al. 2014). Contrary to the inversion frequencies, the near-

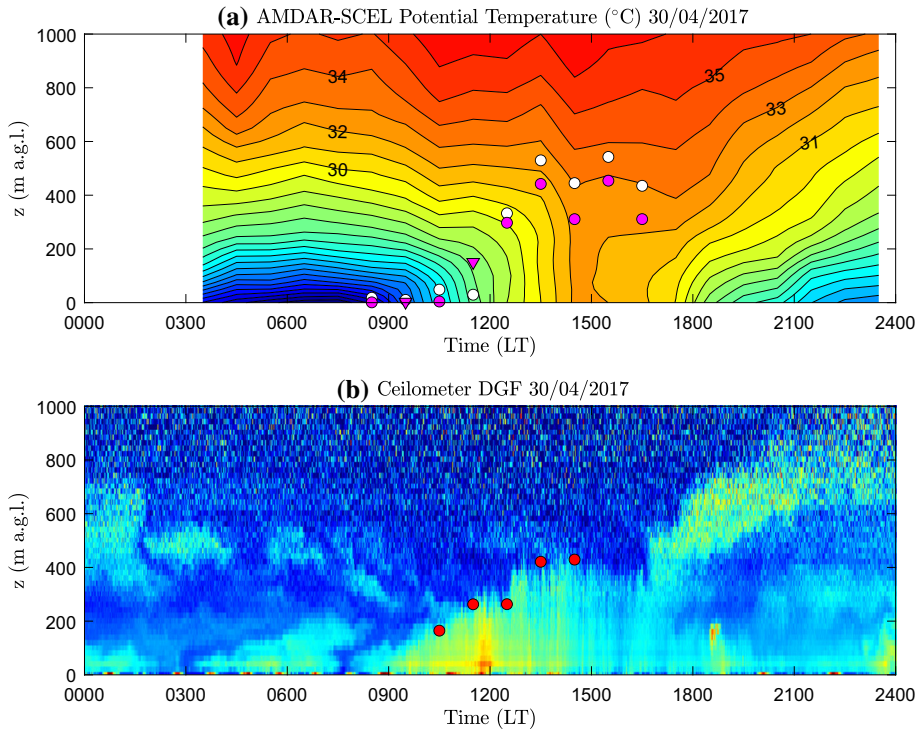


Fig. 7 Example of CBL height determination with different methods for 30 April 2017. **a** Contours of AMDAR potential temperature ($^{\circ}\text{C}$) and CBL height estimated using the parcel (purple symbols) and the bulk Richardson number (white symbols) methods. Triangles denote time-interpolated values. **b** Backscatter intensity of DGF ceilometer (arbitrary units) and CBL height estimated with the method of Muñoz and Undurraga (2010)

neutral layers occur preferentially during daytime in a layer that grows from near the surface in the morning up to ≈ 500 m a.g.l. around 1600 LT, marking the development of the diurnal CBL. The tenuous secondary frequency maximum of near-neutral layers occurring around 1000 m a.g.l. between 1600 and 2100 LT is much more prominent in summer (frequencies $> 40\%$, not shown) and is one feature that appears much more frequently in descent than in ascent soundings (not shown), suggesting a horizontal variation in the stability at these levels that could be caused, for example, by the advection of an elevated CBL from the hills or valleys located to the north of the Santiago valley. However, a better understanding of the non-trivial features found in the stability frequency profiles generated with the AMDAR data (Fig. 6) requires additional detailed analysis and is left for future work.

4.2 Convective-Boundary-Layer Heights

An example of CBL heights diagnosed using the three methods considered is shown in Fig. 7 for 30 April 2017. Panel a shows the time–height evolution of potential temperature obtained from AMDAR data together with the CBL heights derived using the parcel method (purple symbols) and the Ri_b method (white symbols). As the near-surface potential temperature begins to increase in the morning the isentropes become quasi-vertical, signalling the well-mixed character of the CBL developing during daytime. Both methods used to estimate the

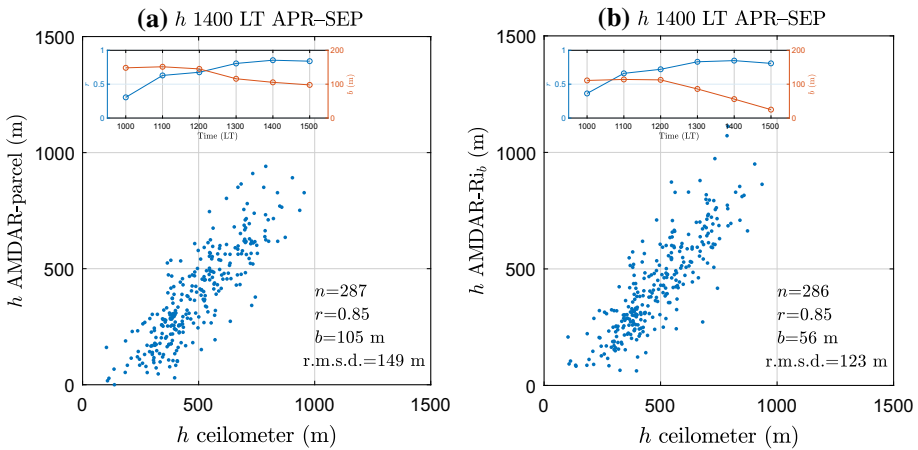


Fig. 8 Scatter diagrams between DGF ceilometer CBL heights at 1400 LT and those derived from AMDAR data using **a** the parcel, and **b** the bulk Richardson methods. Indices in the lower-right corner indicate number of point (n), correlation coefficient (r), mean bias (b), and root-mean squared deviations (r.m.s.d.). Insets show correlations (blue, left scale) and mean biases (red, right scale) for the 1000–1500 LT period in the months from April to September (APR–SEP)

CBL height capture the rapid growth of the mixed layer between 1100 and 1400 LT and the levelling off thereafter, although the Ri_b method produces slightly larger heights than the parcel method in the afternoon. Figure 7b shows the corresponding time–height evolution of backscatter intensity from the DGF ceilometer. During cloud-free days, the intensity of the reflectivity is related to the presence of aerosols in the boundary layer so that the layer with enhanced reflectivity growing from the surface at 0900 LT up to about 400 m around 1500 LT is interpreted as marking the development of the well-mixed CBL. Red circles in this case show the CBL height derived with the methodology of Muñoz and Undurraga (2010). There is a relatively good match between the daytime evolution of the reflectivity and the potential temperature fields of both panels, and though during the morning the CBL heights diagnosed with the three methods differ, all of them level off around 400 ± 100 m in the afternoon.

To generalize the previous results, Fig. 8 shows scatter diagrams between cold-season CBL heights at 1400 LT derived from the ceilometer and those diagnosed with the AMDAR data using the parcel method (panel a) and the Ri_b method (panel b). At this time, the mean bias and the r.m.s.d. show that the Ri_b method height estimates are better related to the ceilometer estimates than those obtained with the parcel method. Moreover, the insets show that while the comparison with ceilometer-derived heights of both methods deteriorates at earlier hours, the Ri_b method is consistently closer to the ceilometer method. The positive bias of mixed-layer heights estimated with ceilometer measurements as compared to heights estimated from vertical temperature and wind profiles is consistent with observations referred to by Seibert et al. (2000). Although none of these methods can be considered the ideal or standard for diagnosing CBL heights, the relatively better agreement of the Ri_b method with the ceilometer method and the larger number of cases that it produces lends support to using its results to study the energy budget of the Santiago CBL in the next section, although in the discussion section we shall briefly mention how the results change when the parcel method is used.

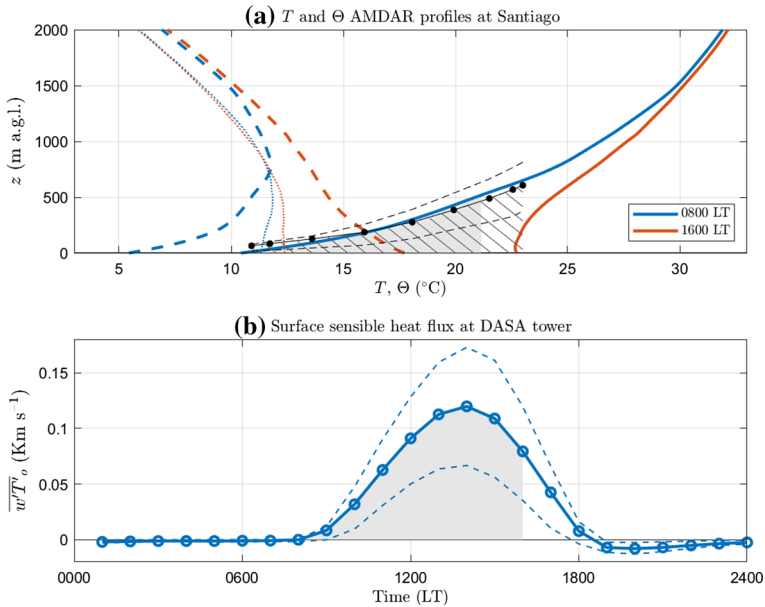


Fig. 9 April–September averages of elements of the daytime heat budget over Santiago. **a** Temperature (dashed) and potential temperature (continuous) AMDAR profiles for 0800 LT (blue) and 1600 LT (red). The fine blue (red) dotted line shows SCSN mean temperature profiles at 0800 LT (2000 LT). The dots on the full black curve represent, from left to right, the mean h and θ values as determined for hours 0800–1600 LT using the Ri_b method. The dashed black lines mark the upper and lower quartiles of h . **b** Mean diurnal cycle of surface sensible heat flux in kinematic units (K m s^{-1}) measured at the DASA tower (solid line with circles) and upper and lower quartiles (dashed lines). The shaded areas in both panels represent the same integrated energy amount. The hatched area in a) represents the integral A of Eq. 4

5 Assessing the Heat Budget of the Santiago Convective Boundary Layer

In this section we explore the suitability of the AMDAR vertical profiles of temperature and ancillary surface data to describe the cold-season, dry-weather daytime energy budget of the Santiago valley CBL. We first explore the averaged elements of the energy budget (Fig. 9) and then turn to its day-to-day variability (Fig. 10). Figure 9a shows mean vertical profiles of temperature and potential temperature at 0800 and 1600 LT. The early morning temperature profile shows the rather deep inversion existing typically by the end of the night over Santiago, extending up to about 700 m a.g.l. The afternoon profile shows a typical free-tropospheric stability above 1500 m a.g.l., a more stable gradient between 500 and 1500 m a.g.l., and a less stable condition below 500 m a.g.l., reflecting the daytime warming of the MoBL. The heat budget is more easily described by the corresponding potential temperature profiles (continuous lines in Fig. 9a). While the daytime warming is more prominent below 500 m a.g.l., there is still warming up to about 1500 m a.g.l. in these averaged profiles. This diurnal warming above 500 m is not present at the coast, as shown by the 0800 and 2000 LT averaged temperature profiles of the SCSN routine radiosondes (fine dotted lines).

One of the important sources of daytime warming of the valley's MoBL is the sensible heat flux supplied by the surface. Figure 9b shows the averaged diurnal cycle of the sensible heat flux measured by the sonic anemometer at the DASA tower. The integral of this flux between

0800 and 1600 LT should partly explain the warming of the temperature profiles shown in Fig. 9a. To illustrate this, in both panels we have shaded corresponding areas of equal energy. It is striking that the surface sensible heat flux appears to explain a large fraction of the heating within the CBL, but explains only about half of the total average daytime warming of the full MoBL (area between blue and red continuous lines in Fig. 9a), pointing to the need for distinguishing between the CBL and the MoBL as indicated in the Introduction. The heating discrepancy noted in the MoBL may be caused by: (1) limitations in the data used to construct Fig. 9, be it the suitability of AMDAR temperature profiles to characterize the average valley’s air mass or of the sensible heat flux data to represent the heat exchange over all the valley’s surface; or (2) additional warming mechanisms like entrainment, subsidence, horizontal advection or radiation.

To dwell further on the possibilities mentioned above, we consider the thermodynamic energy conservation equation for a CBL in the form

$$\frac{\partial \theta}{\partial t} = \frac{\overline{w'T'_o} - \overline{w'T'_h}}{h} + \dot{\theta}_{ad}, \tag{2}$$

where θ is the CBL potential temperature; $\overline{w'T'_o}$ and $\overline{w'T'_h}$ are the turbulent heat fluxes at the surface and at the top of the CBL, respectively; h is the CBL height; and $\dot{\theta}_{ad}$ stands for horizontal temperature advection inside the CBL. Radiative processes are not included in Eq. 2 but are addressed in the discussion section. Subsidence, on the other hand, is absent in Eq. 2 not because it is neglected, but because it does not play a direct role in the energy budget of a well-mixed CBL (Yi et al. 2001; Vila-Guerau de Arellano et al. 2015), its effects being felt through vertical advection of the CBL top and warming and stabilization of the layer above the CBL. For a free convection regime, the entrainment heat flux at the top of the CBL is commonly parametrized as $\overline{w'T'_h} = -\beta \overline{w'T'_o}$, where β is an entrainment factor usually taken as $\beta = 0.2$ (Vila-Guerau de Arellano et al. 2015). Equation 2 can then be rewritten as

$$h \frac{\partial \theta}{\partial t} = (1 + \beta) \overline{w'T'_o} + h \dot{\theta}_{ad}. \tag{3}$$

Integrating between times t_1 and t_2 gives

$$\underbrace{\int_{\theta_1}^{\theta_2} h d\theta}_A = (1 + \beta) \underbrace{\int_{t_1}^{t_2} \overline{w'T'_o} dt}_S + \underbrace{\int_{t_1}^{t_2} h \dot{\theta}_{ad} dt}_{A_{ad}}, \tag{4}$$

where θ_1 and θ_2 are the CBL potential temperatures at times t_1 and t_2 . As indicated, subsequently we call the three integrals in Eq. 4, from left to right, as A , S , and A_{ad} . In the following, we attempt to evaluate the terms in Eq. 4 using the available data to check the physical consistency of the data and to see if this exercise sheds light on the discrepancy mentioned above.

The integral A can be visualized as the area below the curve defined by the co-variation of h and θ along the hours of integration. In the averaged conditions of Fig. 9a we added as a black line the (h, θ) curve constructed with the mean CBL heights and potential temperatures derived from the AMDAR profiles for hours 0800–1600 LT. The hatched area between this curve and the surface represents therefore the energy, A , associated to the daytime warming and growing of this average CBL. This hatched area is about 45% larger than the mean surface sensible heating (shaded area), which could be explained partly by physical processes (e.g., entrainment) or observational issues (e.g., underestimation of surface fluxes).

The day-to-day co-variability of the elements of the heat budget is explored in Fig. 10. First, we compute the total warming in the 0–1500 m layer between hours 0800 and 1600

LT, $A_{0-1500\text{ m}} = \int_{08}^{16} \int_0^{1500\text{ m}} \frac{\partial \theta}{\partial t} dz dt$, and compare it in Fig. 10a with the surface heating, S , derived from the sonic anemometer sensible heat flux data. This comparison does not depend on the estimation of the CBL height and provides a first look at the role of surface heating on the daytime warming of the lower troposphere. Consistent with the averaged conditions of Fig. 9, $A_{0-1500\text{ m}}$ is typically much larger than surface heating by a factor close to 2 on average. Moreover, the modest correlation shows that only a small fraction of the lower-tropospheric daytime warming variability can be explained by the surface heat flux ($\approx 18\%$). Figure 10b compares the terms of Eq. 4 corresponding to CBL warming (A) and surface heating (S). For computing A , the values of h and θ are those derived from AMDAR profiles using the Ri_b method. By considering the warming of just the CBL, surface heating explains now a larger fraction of the warming variability ($\approx 56\%$). While the slope of the best fit to the data (red line) results very close to what is expected for free convection (black line), there is still a considerable dispersion among individual days, some of which show little CBL warming despite relatively large surface sensible heat fluxes (red points). We hypothesize that part of the dispersion is explained by horizontal thermal advection in the CBL and have tested two alternative ways of quantifying this effect with the available data. The first method exploits the different typical paths probed by landing and departing airplanes, as described in Sect. 3.1. As most aircraft departures are towards the south, and most of the approaches are from the north, the difference between descending and ascending temperature profiles may be used to estimate the meridional temperature gradient in the valley. The advective term of Eq. 4 is then computed by

$$A_{\text{ad1}} = \int_{0800}^{1600} \int_0^{h(t)} \left(-V \frac{\theta_d - \theta_a}{L_y} \right) dz dt, \quad (5)$$

where V is the AMDAR meridional wind profile, θ_d and θ_a are the descending and ascending potential temperature profiles, respectively, and L_y is a length scale that goes from 0 at the surface to 35 km at 1000 m a.g.l. and which approximates the typical meridional distance between the descending and ascending paths of the airplanes. The second method to estimate horizontal advection focuses on the possible intrusion into the Santiago valley of the cool coastal ABL existing to the west. In this case, the advective term of Eq. 4 is computed by

$$A_{\text{ad2}} = \int_{0800}^{1600} h \left(-U_p \frac{\theta - \theta_p}{L} \right) dt, \quad (6)$$

where h and θ are the CBL height and temperature values estimated with the Ri_b method, and U_p and θ_p are the zonal wind speed and potential temperature observations at the El Paico station located near the south-western entrance gap of the valley (Fig. 1). The value of the advective length scale, L , that maximizes the correlation between $A - A_{\text{ad2}}$ and S is 60 km and, thus, it approximates the distance between El Paico and the centre of the valley. This second method to estimate advection was already utilized by Muñoz and Undurraga (2010) when performing a first approach to the daytime heat budget of the Santiago valley using the DGF ceilometer data, although at that time there were no surface sensible heat flux data and vertical profiles of temperature available to better constrain the budget.

The scatter plots between S and $A - A_{\text{ad1}}$ and $A - A_{\text{ad2}}$ are shown in Fig. 10c, d, respectively. In both cases, the inclusion of the advective effect appears to correct the anomalous low-warming cases (red points), although the advective term A_{ad1} does not improve the correlation and increases the dispersion between the points as compared to Fig. 10b. The advective correction A_{ad2} , on the other hand, substantially improves the correlation between the CBL warming and the surface heat flux ($\approx 81\%$ of explained variance), suggesting that

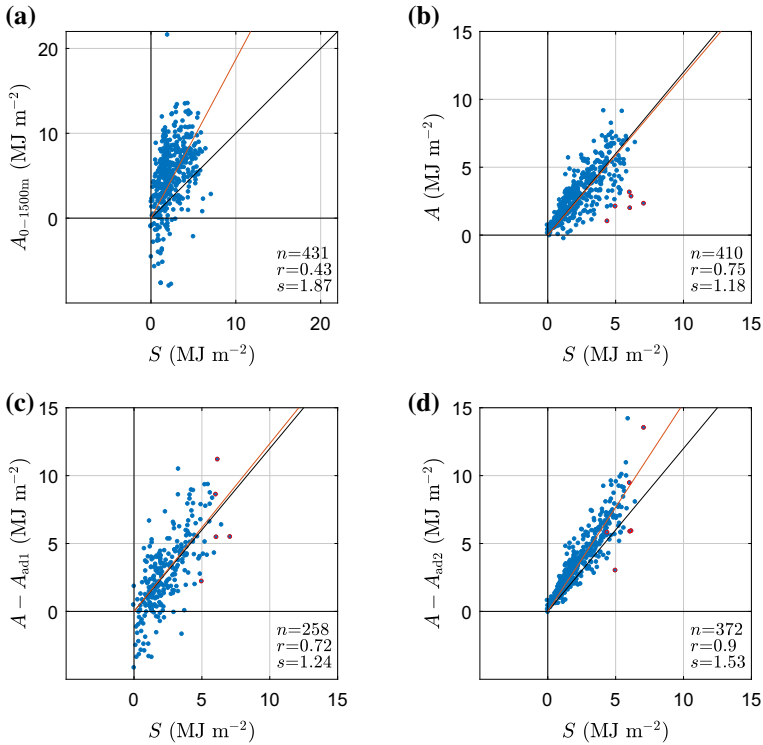


Fig. 10 Scatter diagrams between elements of the daytime energy budget over Santiago for April–September 2017–2019. **a** Surface sensible heat flux integrated between 0800 and 1600 LT (S) and warming area integrated between the surface and 1500 m a.g.l. ($A_{0-1500m}$). Black diagonal indicates the identity line. **b** as **(a)** but the ordinate corresponds to the warming area A of the CBL. **c** as **(b)** but an estimate of low-level advection based on ascent-descent AMDAR temperature differences (A_{ad1}) is used to correct A . **d** as **(b)** but an estimate of low-level advection based on El Paico station data (A_{ad2}) is used to correct A . In **(b)** 6 days with low CBL warming and high surface sensible heat flux have been marked with red points, and their locations indicated also in panels **c** and **d**. Black lines in **(b)**, **(c)**, and **(d)** show the expected relationship between both variables assuming an entrainment factor $\beta = 0.2$ (black). Red lines in all panels show the best linear fit forcing a zero intercept. The number of points (n), correlation coefficient (r) and slope (s) of the zero-intercept best fit are shown in the lower right corner of each panel

intrusion of coastal air is indeed important for the Santiago valley daytime heat budget. Possible reasons for the remaining variance in Fig. 10d and for the larger slope of the best fit (red line) as compared to the expected value from Eq. 4 when the entrainment factor is set to $\beta = 0.2$ (black line) are discussed in the next section. Nevertheless, Fig. 10d suggests that there is considerable physical consistency between AMDAR temperature profiles and the surface sensible heat fluxes used in this work, and that Eq. 2 represents relatively well the energy budget of Santiago’s daytime CBL during the cold season.

6 Discussion

We separate the discussion of our heat budget results into two parts, addressing first the discrepancy between the MoBL daytime warming and surface heating (Figs. 9a, 10a), and

then the relationship between the CBL warming and surface heating (Fig. 10d). In both cases we consider potential data and methodological limitations as well as possible physical mechanisms behind the results.

The comparison between surface heating and daytime warming of the 0–1500 m a.g.l. layer shows that in terms of energy, the latter is typically about twice the former, with large inter-daily variability and little correlation between them. The good validation of AMDAR temperature profiles against radiosondes in the valley (Sect. 3.2.1) makes it hard to attribute the discrepancy to the profile data. Attributing it to the surface sensible heat flux, on the other hand, would demand an improbably large systematic error in these measurements. Moreover, the large correlation in Fig. 10d suggests that the surface sensible heat flux indeed explains a large fraction of the CBL warming variability, so that the small correlation in Fig. 10a points to mechanisms different than surface heating that may be affecting the MoBL daytime warming, especially above the CBL. Among these mechanisms we consider horizontal advection and subsidence, as radiative processes in the very clean air in this subtropical location would produce a cooling effect. A first-order estimation of horizontal advection is gained by using thermal wind arguments on the mean vertical profiles of zonal and meridional winds as deduced from Fig. 5 (similar to those in Fig. 3a). Above 700 m a.g.l. zonal (meridional) winds are positive (negative) and increase (decrease) with height. Applying a thermal wind analysis, we conclude that on average a negative zonal and a positive meridional temperature advection cancel each other in the 700–1500 m a.g.l. layer (not shown). This leaves diurnally varying subsidence as the main process that could explain the daytime warming over Santiago above the CBL. The average conditions of Fig. 9 suggest that at around 700 m a.g.l. a 250 m descent is needed in these 8 h to account for the warming above the CBL, which amounts to a subsidence rate $\approx 0.01 \text{ m s}^{-1}$. Since at the SCSN station, farther from the Andes, this extra daytime warming is not observed (dotted profiles in Fig. 9a), the local and mesoscale topography is probably playing a role in the form, for example, of a mountain–plain circulation (Rotach et al. 2015). In northern Chile, Rutllant et al. (2003) showed that daytime heating of the western slopes of the Andes generates a direct thermal circulation that strengthens the subsidence over the Atacama Desert above the ABL. Through several field campaigns measuring wind profiles in a zonal transect, they used the zonal wind divergence to estimate subsidence rates of several cm s^{-1} . While these values are similar to our estimate, the coastal mean zonal wind profiles at the SCSN station are in our case equal or slightly larger than over Santiago (Fig. 4a), so that the same mechanism is harder to envision here. In central Chile, Garreaud and Rutllant (2003) and Rutllant and Garreaud (2004) showed that during the development of coastal lows, significant lower-tropospheric warming is due to subsidence down the western slope of the Andes. While this process has mainly a synoptic variability, it may be playing a role in the unexplained warming derived from the AMDAR data. Another possibility is compensatory subsidence balancing the anabatic flows exporting air from the valley through the lateral slopes and canyons, as has been reported for several valleys and basins elsewhere, including the Elqui valley, 400 km north of Santiago (Khodayar et al. 2008; Bischoff-Gauß et al. 2008). For a $40 \times 100 \text{ km}^2$ valley like Santiago, a 0.01 m s^{-1} subsidence at its top would correspond to an averaged 1.4 m s^{-1} wind speed through its border if the depth of the outflow layer is 100 m. While these scales are plausible, observations are lacking to establish them more firmly. For now, then, the precise nature of the hypothesized reinforced daytime subsidence cannot be settled and must be left for future modelling and more specific observational studies.

We now turn attention to the comparison between surface heating and CBL daytime warming (corrected by horizontal thermal advection). The large correlation between these terms in Fig. 10d suggests that at least at the inter-daily scale there is physical consistency

between the various datasets used to compute them. Still, the best fit slope (1.53) in Fig. 10d is greater than what can be expected for free convective conditions (1.2) and about 20% of the variance remains unexplained. In what follows we discuss possible factors for these issues.

The difference in the slopes mentioned above may be due to a possible underestimation of surface heating; a possible overestimation of the net CBL warming; or the existence of other physical mechanisms affecting CBL warming. With respect to surface heating, the use of one-point flux measurements to represent the overall valley floor is questionable, but lack of measurements at additional sites made this choice unavoidable. However, as mentioned in Sect. 2.3, the footprint of the measurements corresponds to bare soil in an urban environment, which suggests more an overestimation than an underestimation of the mean flux of the valley. On the other hand, the well-known closure problem of the surface energy balance has been many times attributed to an inability of single-point eddy-covariance methods to account for the effect of sub-mesoscale circulations (Mauder et al. 2020), which could be playing a role here. With respect to the net CBL warming, it is affected by the estimation of the height and temperature of the CBL and by the method to estimate horizontal advection in the CBL. To estimate the boundary-layer height, we considered the parcel and the Ri_b methods, and although we showed heat budget results for just the Ri_b method, conclusions with the parcel method are very similar. A reduction of the CBL warming can be obtained by modifying the parameters of the methods, e.g., reducing the value of Ri_c or of the surface temperature. However, that would be at the expense of lowering the CBL height estimates, which already have a negative bias compared to the independent ceilometer estimates (Fig. 8). The treatment of CBL advection by Eq. 6, on the other hand, is very crude, as quantifying the actual exchange between the coastal ABL and the inland valley calls for a better characterization of the vertical profiles of wind and temperature at the entrance of the valley. Again, the lack of more observations precludes a more refined estimation of this factor at this time.

Beyond observational and methodological limitations, some physical processes may also underlie the non-explained variance and the different slopes in Fig. 10d. For example, the heat budget in Eq. 2 does not include radiative processes within the CBL. Recent studies have shown that solar radiation absorption can be an important term in the heat budget of aerosol-rich convective CBLs (LeMone et al. 2021) and, indeed, Del Hoyo et al. (2020) have shown that the particulate matter content in Santiago is sufficient to significantly reduce solar radiation reaching the surface. How much of this reduction effectively warms the CBL remains to be assessed. Along the same line, the use of a constant $\beta = 0.2$ in Eq. 3 omits the effects of shear-induced mechanical turbulence across the CBL entrainment zone (Fedorovich and Conzemius 2014). While the winds inside the Santiago valley are typically weak, they still may affect the ABL heat budget through this process.

Another factor not included in our analysis is the geometry of the valley, which is known to be important in evaluating valley mass and heat budgets (Whiteman 1990). As shown in Fig. 1, the valley floor that we considered at a nominal 500 m a.s.l. altitude extends in reality from 300 to 800 m a.s.l., which should be taken into account in a more detailed heat budget. The same can be said about our use of single values of CBL heights and temperatures, which could vary in response to the different land covers in the valley. In particular, an urban effect may exist in the central portion of the valley, as suggested by previous studies (Peña 2009; Sarricolea and Martín-Vide 2014; Montaner-Fernández et al. 2020), although these have focused mostly on summer and night-time conditions.

To resolve the issues discussed in this section, future modelling and observational efforts can be proposed. Still, the results here show that the semi-continuous AMDAR profiles and the DASA tower measurements will constitute a useful long-term framework with respect to which such endeavors can be planned and analyzed.

7 Conclusions

The use of AMDAR data in boundary-layer research is still at an early stage, as illustrated by just a handful of papers mentioning the acronym when a search in this journal was made at the time of this writing. As concluded by Rahn and Mitchell (2016), however, the AMDAR data have great potential in the characterization of the lower troposphere around the sites where it is available, especially around busy airports where almost continuous sampling is achieved. In their work, they used AMDAR data to produce a valuable climatology of the coastal ABL in California and a qualitative discussion of the mechanisms behind it. Others have taken advantage of the global coverage of the data to produce comparative climatologies of ABL heights over large regions (Zhang et al. 2020a). In our case we focused on just one airport and one valley to see whether the data permits quantitative analyses of ABL dynamics beyond establishing its height or mean structure. The case studied was the semi-arid Santiago valley located at the foothills of the Andes in subtropical western South America. The topographic confinement of the valley and the large-scale stability dominating its climate are important factors leading to the severe air-pollution problem of Santiago city, strongly modulated by the ABL dynamics. We have analyzed the AMDAR data for the Santiago airport for the period 2017–2019, with an emphasis on non-rainy days within the cold season (April–September). As in previous studies, care has been taken in the preprocessing of the data: filtering out profiles with few data levels, extending profiles to the surface with the aid of a surface station, interpolating in height using the hypsometric equation, etc. The resulting database encompasses 89% of the cold season hours, with less data during the night. The wind and especially the temperature profiles compared very well against occasional radiosondes launched from a site in the valley. Comparison of the AMDAR profiles with routine radiosondes launched at the coast about 100 km west of Santiago show differences at low altitudes due to the very different ABLs probed by each. Comparison with ERA5 reanalyses, on the other hand, are deficient in the lowest 1000 m a.g.l., probably due to the low resolution of the model being unable to reproduce the valley circulation.

The AMDAR soundings produced an unprecedented view of the mean diurnal variation of winds and temperature in the Santiago valley, which up to now had been described with only limited observational means. A rather deep inversion develops during the night reaching up to 700 m a.g.l., which seems to combine the effects of surface radiative cooling and the influence of the regional subsidence inversion. Mean daytime warming and southerly wind acceleration is observed below 800 m a.g.l. with a conspicuous early morning warming of the 500–1000 m a.g.l. layer that is hard to relate directly to surface heating. Daytime CBL heights diagnosed with a simple bulk Richardson method compare relatively well ($r \approx 0.85$) with those obtained from the reflectivity profiles of a ceilometer. They were used to estimate the heating associated with the daytime warming of the CBL and its variability compared well ($r \approx 0.9$) with that of surface sensible heat flux measured with a sonic anemometer at one point in the valley, provided the effect of the advection of the coastal ABL is taken into account. Intriguingly, however, the CBL warming accounts for just half of the mean daytime warming of the deeper MoBL, suggesting that rather intense climatological diurnal subsidence affects the dynamics of the daytime valley MoBL. Possible sources of this subsidence were discussed, including a direct thermal circulation associated with the heating of the western slopes of the Andes and the compensating subsidence induced by upslope winds in the valley, but a more definitive explanation will probably require high-resolution numerical modelling and additional observations. Still, these new questions about the Santiago valley ABL dynamics

prompted by the AMDAR data confirm already that it can indeed be a useful source of information for ABL studies.

Acknowledgements Partial funding for this work was provided by FONDECYT Grant 1170214 of the Chilean Agency for Research and Development ANID. NOAA's Earth System Research Laboratory/Global Systems Division is acknowledged for making AMDAR soundings available. In particular, Dr. William Moninger is thanked for providing assistance with the data numerous times. ERA5 reanalyses were provided by Copernicus Climate Data Store. Operational radiosondes were obtained from the Department of Atmospheric Sciences of the University of Wyoming website. Dirección Meteorológica de Chile (DMC) is acknowledged for the operation of radiosondes and surface meteorological stations used in this study. Mrs. Juan Quintana, Gastón Torres, and Marcelo Corral kindly helped with the access to DMC data. We thank three anonymous reviewers for constructive comments and suggestions that greatly improved this work.

Data availability The raw data analysed in the study are available in the websites mentioned in the text.

Open Access This article is licensed under a Creative Commons Attribution 4.0 International License, which permits use, sharing, adaptation, distribution and reproduction in any medium or format, as long as you give appropriate credit to the original author(s) and the source, provide a link to the Creative Commons licence, and indicate if changes were made. The images or other third party material in this article are included in the article's Creative Commons licence, unless indicated otherwise in a credit line to the material. If material is not included in the article's Creative Commons licence and your intended use is not permitted by statutory regulation or exceeds the permitted use, you will need to obtain permission directly from the copyright holder. To view a copy of this licence, visit <http://creativecommons.org/licenses/by/4.0/>.

References

- Bischoff-Gauß I, Kalthoff N, Khodayar S, Fiebig-Wittmaack M, Montecinos S (2008) Model simulations of the boundary-layer evolution over an arid Andes valley. *Boundary-Layer Meteorol* 128:357–379
- Bosveld FC, Beljaars ACM (2001) The impact of sampling rate on eddy-covariance flux estimates. *Agric For Meteorol* 109:39–45
- Bustos E, Meza FJ (2015) A method to estimate maximum and minimum air temperature using MODIS surface temperature and vegetation data: application to the Maipo Basin, Chile. *Theor Appl Climatol* 120:211–226
- Cardinali C, Isaksen L, Andersson E (2003) Use and impact of automated aircraft data in a global 4DVAR data assimilation system. *Mon Weather Rev* 131:1865–1877
- De Wekker SFJ, Kossmann M (2015) Convective boundary layer heights over mountainous terrain—a review of concepts. *Front Earth Sci* 3:1–22
- Del Hoyo M, Rondanelli R, Escobar R (2020) Significant decrease of photovoltaic power production by aerosols. The case of Santiago de Chile. *Renew Energy* 148:1137–1149
- Ding J, Zhuge XY, Wang Y (2015) Evaluation of Chinese aircraft meteorological data relay (AMDAR) weather reports. *J Atmos Ocean Technol* 32:982–992
- Ding J, Zhuge XY, Li X, Yuan Z, Wang Y (2018) Evaluation of accuracy of Chinese AMDAR data for 2015. *J Atmos Ocean Technol* 35:943–951
- Drüe C, Hauf T, Hoff A (2010) Comparison of boundary-layer profiles and layer detection by AMDAR and WTR/RASS at Frankfurt airport. *Boundary-Layer Meteorol* 135:407–432
- Emeis S, Schäfer K, Munkel C (2008) Surface-based remote sensing of the mixing-layer height—a review. *Meteorol Z* 17:621–630
- Fedorovich E, Conzemius R (2014) Effects of wind shear on the atmospheric convective boundary layer structure and evolution. *Acta Geophys* 56:114–141
- Garreaud RD (2013) Warm winter storms in Central Chile. *J Hydrometeorol* 14:1515–1534
- Garreaud RD, Rutllant JA (2003) Coastal lows along the subtropical west coast of South America: numerical simulation of a typical case. *Mon Weather Rev* 131:891–908
- Garreaud RD, Rutllant JA, Fuenzalida H (2002) Coastal lows along the subtropical west coast of South America: mean structure and evolution. *Mon Weather Rev* 130:75–88
- Gramsch E, Cáceres D, Oyola P, Reyes F, Vásquez Y, Rubio MA, Sánchez G (2014) Influence of surface and subsidence thermal inversion on PM_{2.5} and black carbon concentration. *Atmos Environ* 98:290–298

- Hersbach H, Bell B, Berrisford P, Biavati G, Horányi A, Muñoz Sabater J, Nicolas J, Peubey C, Radu R, Rozum I, Schepers D, Simmons A, Soci C, Dee D, Thépaut JN (2018) ERA5 hourly data on single levels from 1979 to present. Copernicus Climate Change Service (C3S) Climate Data Store (CDS), Technical Report
- Kalthoff N, Bishoff-Gauß I, Fiebig-Wittmaack M, Fiedler F, Thürauf J, Novoa E, Pizarro C, Castillo R, Gallardo L, Rondanelli R, Kohler M (2002) Mesoscale wind regimes in Chile at 30 S. *J Appl Meteorol* 41:953–970
- Khodayar S, Kalthoff N, Fiebig-Wittmaack M, Kohler M (2008) Evolution of the atmospheric boundary-layer structure of an arid Andes valley. *Meteorol Atmos Phys* 99:181–198
- Kljun N, Calanca P, Rotach MW, Schmid HP (2015) A simple two-dimensional parameterisation for flux footprint prediction (FFP). *Geosci Model Dev* 8(8):3695–3713
- Koutrakis P, Sax SN, Sarnat JA, Coull B, Demokritou P, Oyola P, Garcia J, Gramsch E (2005) Analysis of PM₁₀, PM_{2.5}, and PM_{2.5-10} concentrations in Santiago, Chile, from 1989 to 2001. *J Air Waste Manag Assoc* 55:342–351
- Lehner M, Rotach MW (2018) Current challenges in understanding and predicting transport and exchange in the atmosphere over mountainous terrain. *Atmosphere* 9:1–28
- LeMone MA, Angevine WM, Dudhia J (2021) The role of radiation in heating the clear-air convective boundary layer: revisiting CASES-97. *Boundary-Layer Meteorol* 178:341–361
- Mauder M, Foken T, Cuxart J (2020) Surface-energy balance closure over land: a review. *Boundary-Layer Meteorol* 177:395–426
- Moninger WR, Mamrosh RD, Pauley PM (2003) Automated meteorological reports from commercial aircraft. *Bull Am Meteorol Soc* 84:203–216
- Montaner-Fernández D, Morales-Salinas L, Sobrino J, Cárdenas-Jirón L, Huete A, Fuentes-Jaque G, Pérez-Martínez W, Cabezas J (2020) Spatio-temporal variation of the urban heat island in Santiago, Chile during summers 2005–2017. *Remote Sens* 12:3345
- Muñoz RC (2012) Relative roles of emissions and meteorology in the diurnal pattern of urban PM₁₀: analysis of the daylight saving time effect. *J Air Waste Manag Assoc* 62:642–650
- Muñoz RC, Corral MJ (2017) Surface indices of wind, stability, and turbulence at a highly polluted urban site in Santiago, Chile, and their relationship with nocturnal particulate matter concentrations. *Aerosol Air Qual Res* 17:2780–2790
- Muñoz RC, Undurraga AA (2010) Daytime mixed layer over the Santiago basin: description of two years of observations with a lidar ceilometer. *J Appl Meteorol Climatol* 49:1728–1741
- Petersen RA (2016) On the impact and benefits of AMDAR observations in operational forecasting. Part I: a review of the impact of automated aircraft wind and temperature reports. *Bull Am Meteorol Soc* 97:585–602
- Peña MA (2008) Relationships between remotely sensed surface parameters associated with the urban heat sink formation in Santiago, Chile. *Int J Remote Sens* 29:4385–4404
- Peña MA (2009) Examination of the land surface temperature response for Santiago, Chile. *Photogramm Eng Remote Sens* 75:1191–2000
- Rahn DA, Mitchell CJ (2016) Diurnal climatology of the boundary layer in southern California using AMDAR temperature and wind profiles. *J Appl Meteorol Climatol* 55:1123–1137
- Rotach MW, Gohm A, Lang MN, Leukauf D, Stiperski I, Wagner JS (2015) On the vertical exchange of heat, mass, and momentum over complex, mountainous terrain. *Front Earth Sci* 3:1–14
- Rutllant JA, Garreaud RD (1995) Meteorological air pollution potential for Santiago, Chile: towards an objective episode forecasting. *Environ Monit Assess* 34:223–244
- Rutllant JA, Garreaud RD (2004) Episodes of strong flow down the western slope of the subtropical Andes. *Mon Weather Rev* 132:611–622
- Rutllant JA, Fuenzalida H, Aceituno P (2003) Climate dynamics along the arid northern coast of Chile: the 1997–1998 dinámica del clima de la región de Antofagasta (DICLIMA) experiment. *J Geophys Res* 108:4538
- Sarricolea P, Martín-Vide J (2014) El estudio de la isla de calor urbana de superficie del área metropolitana de Santiago de Chile con imágenes Terra-MODIS y análisis de componentes principales. *Rev Geog Norte Grande* 57:123–141
- Scaff L, Rutllant JA, Rahn D, Rondanelli R, Gascoín S (2017) Meteorological interpretation of orographic precipitation gradients along an Andes west slope basin at 30 S (Elqui valley, Chile). *J Hydrometeorol* 18:713–727
- Seibert P, Beyrich F, Gryning SE, Joffre S, Rasmussen A, Tercier P (2000) Review and intercomparison of operational methods for the determination of the mixing height. *Atmos Environ* 34:1001–1027
- Seidel DJ, Ao CO, Li K (2010) Estimating climatological planetary boundary layer heights from radiosonde observations: comparison of methods and uncertainty analysis. *J Geophys Res* 115(D16):113

- Stull R (1988) An introduction to boundary layer meteorology. Kluwer Academic Press, Dordrecht
- Tennekes H (1973) A model of the dynamics of the inversion above a convective boundary layer. *J Atmos Sci* 30:558–567
- Vila-Guerau de Arellano J, van Heerwaarden CC, van Stratum BJH, van den Dries K (2015) Atmospheric boundary layer—integrating air chemistry and land interactions. Cambridge University Press, Cambridge
- Vogelezang DHP, Holtslag AAM (1996) Evaluation and model impacts of alternative boundary-layer height formulations. *Boundary-Layer Meteorol* 81:245–269
- Whiteman CD (1990) Observations of thermally developed wind systems in mountainous terrain. In: Blumen W (ed) Atmospheric processes over complex terrain. American Meteorological Society, Providence
- WMO (2017) AMDAR observing system newsletter. World Meteorological Organization, Technical Report Volume, p 13
- Yi C, Davis KJ, Berger BW (2001) Long-term observations of the dynamics of the continental planetary boundary layer. *J Atmos Sci* 58:1288–1299
- Zardi D, Whiteman CD (2013) Diurnal mountain wind systems. In: De Wekker SFJ, Snyder BJ, Chow FK (eds) Mountain weather research and forecasting. American Meteorological Society, Providence
- Zhang Y, Li D, Lin Z, Santanello JA, Gao Z (2019) Development and evaluation of a long-term data record of planetary boundary layer profiles from aircraft meteorological reports. *J Geophys Res* 124:2008–2030
- Zhang Y, Sun K, Gao Z, Pan Z, Shook MA, Li D (2020a) Diurnal climatology of planetary boundary layer height over the contiguous United States derived from AMDAR and reanalysis data. *J Geophys Res* 125 e2020JD032803
- Zhang Y, Wang L, Santanello JA, Pan Z, Gao Z, Li D (2020) Aircraft observed diurnal variations of the planetary boundary layer under heat waves. *Atmos Environ* 235(104):801

Publisher's Note Springer Nature remains neutral with regard to jurisdictional claims in published maps and institutional affiliations.